

Title	Low-dimensional, hinged bar-code metal oxide layers and free-standing, ordered organic nanostructures from turbostratic vanadium oxide
Authors	O'Dwyer, Colm;Lavayen, Colm;Fuenzalida, David;Lozano, Harold;Santa-Ana, María A.;Benavente, Eglantina;Gonzalez, Guillermo;Sotomayor Torres, Clivia M.
Publication date	2008-06-05
Original Citation	O'Dwyer, C., Lavayen, V., Fuenzalida, D., Lozano, H., Santa Ana, M. A., Benavente, E., Gonzalez, G. and Sotomayor Torres, C. M. (2008) 'Low-dimensional, hinged bar-code metal oxide layers and free-standing, ordered organic nanostructures from turbostratic vanadium oxide'. <i>Small</i> , 4(7), pp. 990-1000. <a href="http://dx.doi.org/10.1002/sml.200701014">http://dx.doi.org/10.1002/sml.200701014</a>
Type of publication	Article (peer-reviewed)
Link to publisher's version	<a href="http://dx.doi.org/10.1002/sml.200701014">10.1002/sml.200701014</a>
Rights	© 2008 Wiley-VCH Verlag GmbH & Co. KGaA, Weinheim. This is the peer reviewed version of the following article: O'Dwyer, C. et al., [2008]. Low-dimensional, hinged bar-code metal oxide layers and free-standing, ordered organic nanostructures from turbostratic vanadium oxide. <i>Small</i> , 4, 990-1000, which has been published in final form at <a href="http://dx.doi.org/10.1002/sml.200701014">http://dx.doi.org/10.1002/sml.200701014</a> . This article may be used for non-commercial purposes in accordance with Wiley Terms and Conditions for Self-Archiving. <a href="http://olabout.wiley.com/WileyCDA/Section/id-820227.html#terms">http://olabout.wiley.com/WileyCDA/Section/id-820227.html#terms</a>
Download date	2024-04-26 08:18:07
Item downloaded from	<a href="https://hdl.handle.net/10468/2831">https://hdl.handle.net/10468/2831</a>



# UCC

**University College Cork, Ireland**  
Coláiste na hOllscoile Corcaigh

DOI: 10.1002/sml.200((.....))

# Low-Dimensional Hinged Barcode Metal Oxide and Free-Standing Ordered Organic Nanostructures from Turbostratic Vanadium Oxide

C. O'Dwyer\*, V. Lavayen, D. Fuenzalida, H. Lozano, M. A. Santa Ana, E. Benavente, G. González, C. M. Sotomayor Torres

*Both low-dimensional barcoded metal-oxide layers that exhibit molecular hinging and free-standing organic nanostructures can be obtained from unique nanofibers of vanadium oxide (VO<sub>x</sub>), successfully synthesized by a simple chemical route using an ethanolic solution of vanadium pentoxide xerogel and dodecanethiol resulting in a double bi-layered laminar turbostratic structure. The formation of vanadium oxide nanofibers is observed after hydrothermal treatment of the thiol-intercalated xerogel resulting in typical lengths in the range 2-6 μm and widths of ~50-500 nm. We observe concomitant hinging of the flexible nanofiber lamina at periodic hinge points in the final product on both the nanoscale and molecular level. Barcoded nanofibers comprise alternating segments of organic(thiols)-inorganic(VO<sub>x</sub>) material and are amenable to segmented, localised metal nanoparticle docking. Under certain conditions free standing bi-layered organic nanostructures are realized.*

## Keywords:

- Nanofibers
- Hydrothermal synthesis
- Intercalation
- Vanadium
- Nanostructures

## 1. Introduction

One-dimensional nanomaterials, such as nanotubes,<sup>[1]</sup> nanowires,<sup>[2-4]</sup> and nanobelts or nanoribbons<sup>[5,6]</sup> have attracted considerable attention in the past decade because of their novel and useful physical properties, leading to numerous applications. Besides the use of 1D metal-oxide nanostructures as functional components in electronics and interconnects in dense, high-speed circuits, they also find application in ultra-small sensors, optical elements for optoelectronics, non-linear optical converters and information storage devices.<sup>[7,8]</sup> Due to the versatile chemical properties often modulable by changes in the oxidation state of the metal coordination sphere and a judicious choice of intercalated organic guest molecules, metal-oxide nanostructures may lead to a variety of products and tuneable materials.<sup>[9,10]</sup> Vanadium oxide has attracted considerable attention not only as a Li<sup>+</sup> intercalation host due to its layered structure, but depending on the nature of the species present in the reaction medium, these vanadium oxides may exhibit a wide range of morphologies.

[\*] Dr C. O'Dwyer  
Tyndall National Institute  
University College Cork  
Lee Maltings, Cork (Ireland)  
Fax: (+353)490-4467  
E-mail: [colm.odwyer@tyndall.ie](mailto:colm.odwyer@tyndall.ie)

Prof. C. M. Sotomayor Torres  
Institute for Research and Advanced Studies, ICREA, 08010  
Barcelona and  
Catalan Institute of Nanotechnology, Edifici CM7, Campus  
Universitat Autònoma de Barcelona, 08193 Bellaterra,  
Barcelona (Spain)

Dr V. Lavayen, D. Fuenzalida, H. Lozano, Dr M. A. Santa Ana,  
Prof. G. González  
Department of Chemistry, Faculty of Science,  
Universidad de Chile, Santiago (Chile)

Prof. E. Benavente  
Department of Chemistry, Universidad Tecnológica  
Metropolitana, Santiago (Chile)

Nanostructures with lamellar structure,<sup>[8]</sup> scrolled nanotubes,<sup>[11,12]</sup> nanowires,<sup>[13]</sup> nanorods<sup>[14]</sup> and nanourchin<sup>[15,16]</sup> have been realized using a variety of organic templates during synthesis. Each of these structures relies on the structural direction provided by intercalated or adsorbed organic molecules.

The interest in the role of membrane curvature is profound; its understanding is only starting to become important in nanobiological materials, due to the ubiquitous nature of curved lipid layers/membranes in living systems<sup>[17,18]</sup> and it results in unique nanotubular structures from curved lamellar metal-oxides. The curvature can have a significant effect on bilayer structure and recent experiments demonstrated curvature directed segregation of lipid mixtures in nonplanar membranes.<sup>[19,20]</sup> The need to understand how curvature is induced and affects the physical properties of layers and membranes in crucial is such systems.<sup>[21,22]</sup> When the main body of a nanostructure such as lamellar vanadium oxide nanofibers, comprises longitudinally segmented sections, these heterostructured nanofibers can provide barcode-like docking points for a wide range of moieties such as functionalizable organic ligands, and metal or optically active nanoparticle incorporation.<sup>[12]</sup> Each segment can thus serve as a recognition site or adsorption region. This attribute, among many others, accounts for the growing interest in barcoded layered materials in bioanalytics, diagnostics and separations, for example<sup>[23,24]</sup> and even opportunities for assembling functional architectures with lipid membrane-mediated biorecognition.<sup>[25]</sup> End, side and segment-specific molecular recognition can facilitate end-to-end, side-to-side and end-to-side assembly of different nanostructure architectures, such as chains, bundles and crossbars by taking advantage of, for example, magnetic interactions with susceptible metal nanoparticles in the inter-segment voids.

The advantage of template-based growth methods is the ability of fabricating unidirectionally aligned and uniformly sized nanostructured arrays and further study and development of template-based growth of prospective multifunctional nanostructures is obviously of significant importance. Due to high efficiency, simplicity and versatility of their synthesis, bottom-up approaches using surfactants or micelles as the regulating structural directors or templates can be readily employed in the fabrication of low-dimensional nanostructures. Recent developments in chemical nanolocomotion have raised the intriguing possibility of assembling nanomachines with metal nanorods;<sup>[26,27]</sup> nanostructured constructs displaying any form of either flexibility of discrete compositional variations along their length are only beginning to be discovered.<sup>[28]</sup> Further scientific and technological advances in the application of low-dimensional nanostructures in functional devices depend on the ability to organize them<sup>[29]</sup> in complex one- or multi-dimensional functional architectures.

Here, we detail the successful synthesis and realization of multifunctional laminar vanadium oxide intercalates. This turbostratic thiol-functionalized VO<sub>x</sub> nanofiber exhibits morphological variations such as periodic barcoding by longitudinal modulation of metal-oxide due to periodic organic-inorganic segmentation, delamination to form free-standing molecular bilayer films and curvature-induced

hinging under hydrothermal conditions on the nanoscale and molecular level.

## 2. Results and Discussion

### 2.1. Thiol-Templated and Structurally Directed Bilayered VO<sub>x</sub> Nanocomposite

The formation of vanadium oxide nanofibers was achieved by hydrothermal treatment of the precursor composed of an inorganic-organic laminar nanocomposite, vanadium pentoxide xerogel V<sub>2</sub>O<sub>5</sub>·*n*H<sub>2</sub>O, and dodecanethiol (DDT) resulting in a VO<sub>x</sub>-(DDT)<sub>0.27</sub> nanocomposite. The X-ray powder diffraction patterns of both the xerogel and the nanocomposite prior to HT are shown in Figure 1a. We observe that the VO<sub>x</sub>-(DDT)<sub>0.27</sub> exhibits a set of {00*l*} peaks characteristic of the formation of a bi-layer laminar phase and evidence for the formation of a crystalline matrix.

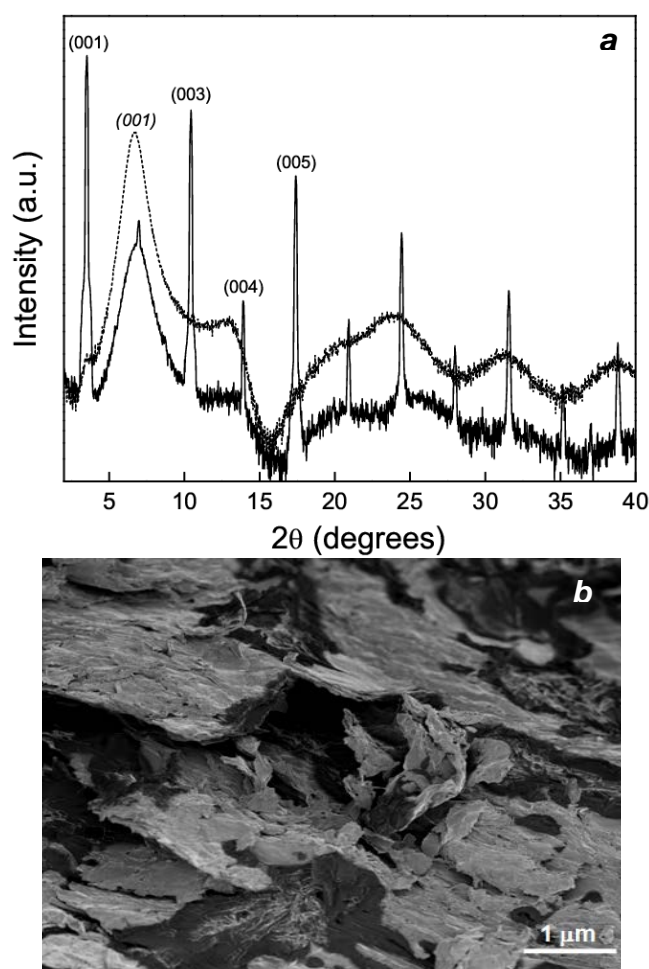


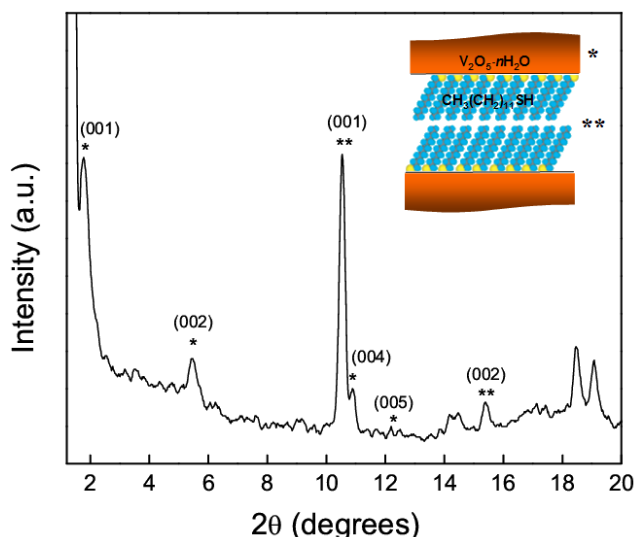
Figure 1. a) X-ray powder diffraction patterns of the (---) VO<sub>x</sub>-(DDT)<sub>0.27</sub> nanocomposite product prior to HT and (···) V<sub>2</sub>O<sub>5</sub>·*n*H<sub>2</sub>O xerogel. The diffraction peaks were indexed on the basis of a two-dimensional square lattice with *a* = 0.611 nm, indicating high structural order of the thiol-vanadate bilayers. b) FESEM image of the VO<sub>x</sub>-(DDT)<sub>0.27</sub> nanocomposite product prior to HT showing its bulk laminarity.

The interlaminar distance is measured to be 2.5 nm from the (001) Bragg reflection. The degree of laminar crystallinity is reflected by the observation of eleventh order

{00l} reflections for this nanocomposite within the experimental  $2\theta$  range of  $0-40^\circ$ . By comparison, the interlaminar spacing of the monoclinic ( $a_0 = 1.1964$  nm,  $b_0 = 0.4697$  nm,  $c_0 = 0.5324$  nm; Space Group =  $c2/c$ )  $V_2O_5 \cdot nH_2O$  xerogel is calculated to be 1.27 nm from its respective (001) Bragg reflection and displays a lower degree of long-range laminarity. The diffraction pattern for the nanocomposite is consistent with the intercalation of the thiol surfactant template into the laminar matrix and indicates that the framework of the host xerogel is preserved, coherent with a topotactic reaction. In particular, the structure permits thiol molecules to be embedded between the layers in an ordered fashion, leading to the formation of the quasi-crystalline  $VO_x-(DDT)_{0.27}$  phase. The laminar morphology of the product is clearly observed even on the macro-scale as evidence by the FESEM image of the product (Figure 1b). It is apparent from the micrograph that the overall morphology is that of a bulk laminar compound.

There is a notable absence of a high intensity (002) reflection from the xerogel diffraction pattern (more observable on the logarithmic scale in Figure 1a) consistent with its arrangement as a double bi-layered product where two vanadate layers are bound by a bi-layered surfactant<sup>[7,16]</sup> and this arrangement is stacked periodically back-to-back. We also observe similarly low intensities for the {00l} peaks, where  $l = 2, 4, 6, \dots, 2(n - 1)$ ;  $n \in \mathbb{N}$ .

The measured interlaminar distance of 2.5 nm, which is larger than the dodecanethiol molecular length ( $CH_3(CH_2)_{11}SH \approx 1.87$  nm), implies a double layer of the thiol oriented either perpendicularly to the  $VO_x$  planes with interdigitated alkyl chains, or forming an angle with them, as previously reported.<sup>[16]</sup> The values suggest that the intercalated surfactant adopts a tilted bi-layer structure, a well-documented ordering for self-assembled monolayers of



thiols.<sup>[34,35]</sup>

**Figure 2.** X-ray powder diffraction pattern of the  $VO_x-(DDT)_{0.27}$  nanocomposite product after HT. (\*) Bi-laminar diffraction from the vanadium oxide nanofibers. (\*\*) Diffraction contribution from the intercalated organic bi-layer. (Inset): Schematic of the double bi-layered system highlighting each contributory bilaminar region to the diffraction pattern.

X-ray diffraction analysis was also conducted on the nanocomposite after HT. As observed in the diffraction pattern in Figure 2. HT treatment of the reaction mixture leads to the formation of a pure mesophase formed by a laminar species (*vide infra*) exhibiting two phases: one with an overall laminar distance of 4.9 nm, identified as orthorhombic  $V_2O_5$ <sup>[36]</sup> and a second phase that exhibits a laminar tendency with an associated laminar thickness of 3.9 nm. As observed for the vanadate lamina, a low (002) diffraction intensity confirms the bi-layered structure of the intercalated organic layer. This second phase is identified as the bi-layer thiol surfactant whose theoretical bi-layer length (as measured from two juxtaposed head-tail molecules) is 3.74 nm. The high intensity phase (\*) has thus the value of 4.9 nm for the overall interlaminar spacing of the nanocomposite and that of the interlaminar length of the surfactant.<sup>[37]</sup> The difference between measured and theoretical molecular bi-layers' length is due to the well-documented uptake of water molecules<sup>[38]</sup> within the vanadate lamina of the xerogel verified here from Fourier transform infrared (FTIR) measurements, as outlined next.

The infra-red vibrational spectrum obtained for the laminar  $VO_x-(DDT)_{0.27}$  nanofibers (Figure 3) highlights key vibrational characteristics of the intercalated lamina; by comparison, previous reports<sup>[39]</sup> have shown that the  $V_2O_5$  xerogel displays three principal absorption peaks at 530, 765, and  $1012\text{ cm}^{-1}$ . The FTIR measurements in Figure 3 however, exhibit four characteristic vibrational bands. Spectral analysis shows that these frequencies correspond to the V=O bond of the vanadyl oxygen at  $\sim 1008\text{ cm}^{-1}$ , a wide asymmetric V-O-V stretching band with a maximum at  $756\text{ cm}^{-1}$ , and a symmetric V-O-V stretching ( $525\text{ cm}^{-1}$ ) mixed with deformation vibrations of the vanadium-oxygen polyhedra, respectively.<sup>[40]</sup>

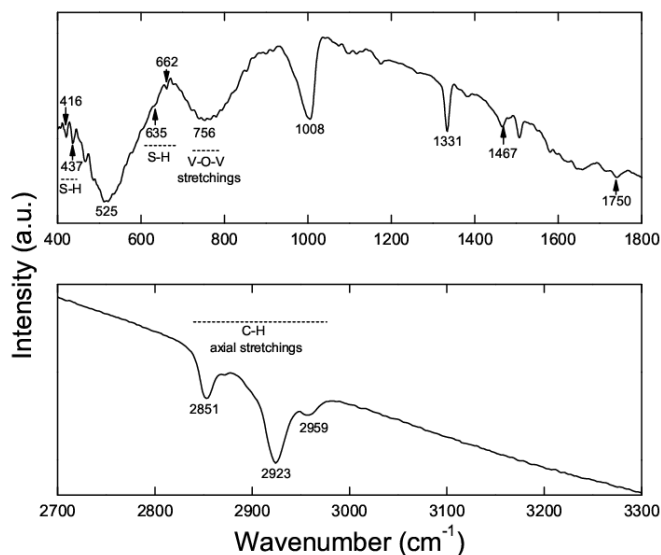


**Figure 3.** FTIR transmittance spectrum, averaged from 300 scans, of the  $VO_x-(DDT)_{0.27}$  nanocomposite product after HT. The spectra were acquired from bulk samples of nanofibers with different respective orientations to the incident probe beam.

The band at  $\sim 1008\text{ cm}^{-1}$  corresponds to the vibrational V=O stretching mode (vanadyl oxygen). We have estimated interatomic distances in this wavenumber range

corresponding to the presence of the distorted pentavalent orthorhombic  $\gamma$ - $V_2O_5$  conformation yielding an associated V=O bond length of 0.155 nm.<sup>[11]</sup> This observation implies that a distortion of the monoclinic vanadate lamina by deformation of the vanadium-oxygen polyhedra, to that of orthorhombic vanadate occurs during HT and influenced by the presence of the thiol molecular template. The nanotube walls are composed of vanadium oxo-anions with either a neutral or negative charge. The presence of  $V^{5+}$  neutralizes this charge if present;  $V^{4+}$  does not. Consequently, the total anion charge on the nanotube walls is a direct function of the  $V^{4+}$  content. As the thiol surfactant used in this work is the structural template and also anionic, greater quantities of  $V^{4+}$  does not necessarily result in more surfactant binding. As the associated electrostatic interaction is much stronger than dative bonding between neutral  $V^{5+}$  sites and amine head groups,<sup>[41]</sup> select areas on any nanofibers that contain high quantities of quadravalent vanadium are thus susceptible to delamination because of reduced surfactant-vanadate binding interactions.

Intense bands resulting directly from surfactant molecules are observed at 2959, 2923 and 2851  $cm^{-1}$ , and are related to the axial stretching of the aliphatic C-H of the methyl and methylene groups. Vibrational spectroscopy has been used extensively to probe the conformation and organization of alkyl chain assemblies. The frequency and line-shape of the stretching and bending vibrational modes of the  $CH_2$  and  $CH_3$  groups are sensitive to the *gauche* to *trans* conformer ratio of the alkyl chains. The methylene stretching modes, for example, shift from lower frequencies characteristic of the highly ordered all-*trans* conformation to higher frequencies and increased line-width as the number of *gauche* conformers in the chain increases. For an all-*trans* alkyl chain, as in the case of crystalline *n*-alkanes, the symmetric and anti-symmetric stretching frequencies are typically in the range 2846-2849 and 2916-2919  $cm^{-1}$ , respectively.<sup>[42]</sup> With a greater number of *gauche* defects this range blue-shifts to 2850-2854 and 2921-2925  $cm^{-1}$  as we observe in Figure 3. These spectroscopic observations show that even in the absence of intermolecular interactions, weak adhesive interactions are sufficient to cause methylene chains to adopt an all-*trans* (solid-like) configuration in the vicinity of a confining surface while accommodating a low density of alkyl chains with *gauche* defect (liquid-like) conformations. A detectable *gauche* defect vibrational contribution to the measured signal can only indicate a greater freedom of movement of the interlayer methylene groups resulting from a less-

ordered packing of the thiols; hinging, bending and shearing are potentially allowed.

Other notable bands are located at 1467  $cm^{-1}$ , related to in-plane symmetric angular deformations of the  $CH_2$  groups, as well a relatively weak band at 721  $cm^{-1}$  corresponding to the C-H bending mode of the methylene groups in the surfactant template. The H-O-H vibrational modes typically found<sup>[43]</sup> in the wavenumber region 3890-3640  $cm^{-1}$  were not observed, however a weak signal with a maximum at 1750  $cm^{-1}$  indicates a detectable presence of remnant water molecules within  $VO_x$ -(DDT)<sub>0.27</sub> nanocomposite<sup>[44]</sup> after HT. The presence of the lateral S-H stretching vibration mode is not detected in the range 2600-2550  $cm^{-1}$ , but between 700-600  $cm^{-1}$  we observe very weak signals from the C-S stretching vibration mode at 662 and 635  $cm^{-1}$ . The absence of the lateral stretching mode and the weakness in intensity of the vertical stretching modes indicates solid confinement and adsorption within the interlaminar spacing and almost no detectable 'wobble' of the alkyl chain head-group at the adsorption site. Structural defects are confined between the center and the tail of the alkyl chain.

## 2.2. Turbostratic Barcoded Inorganic-Organic Morphology and Molecular Hinging

Further structural characterization of the nanofibers was performed using transmission electron microscopy (TEM) (Figure 4a,b), showing low magnification TEM images of the nanofibers with different respective orientations, *i.e.* side and plan view perspectives.

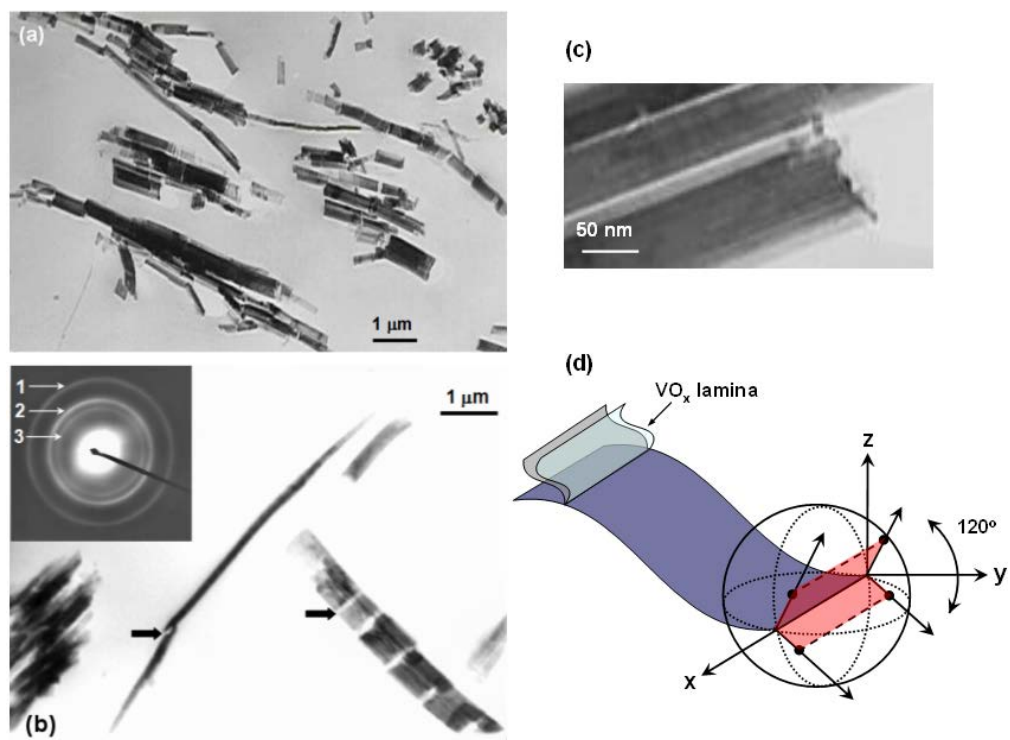


**Figure 4.** a) Bright field TEM images of fully developed, bulk, multilayer  $VO_x$ -(DDT)<sub>0.27</sub> nanofibers after cooling to room temperature after HT. b) Plan and side-view profile TEM images of the nanofibers. Arrows in b) highlight hinge points. (Inset b): Associated bulk electron diffraction pattern of the nanofibers. c) Cross-sectional TEM image of the nanofiber highlighting the organic (bright)-inorganic (dark) barcoded bi-phase structure. d) Schematic representation of the observed hinging and bending vectors of the nanofiber lamina.



The measurements reveal that the high aspect ratio nanofibers of vanadium pentoxide have lengths typically in the range 2-6  $\mu\text{m}$  and plan view widths in the range 50-500 nm. A feature common to all synthesized nanofibers is the quasi-periodic hinging points perpendicular to the long axis of the fiber, (Figure 4b) and the zig-zag nanofibers seen in (Figure 4a) formed by segments of the nanofibers having their long axes at different respective angular positions. Selected area electron diffraction measurements (inset to Figure 4b) indicate that the vanadate constituent of the fibers is orthorhombic  $\text{V}_2\text{O}_5$  with reconstructed lattice parameters of  $a_0 = 1.152$  nm,  $b_0 = 0.356$  nm,  $c_0 = 0.437$  nm; Space Group =  $Pmmn$ . The bulk ED pattern shows prominent polycrystalline diffraction rings (1, 2, and 3) with  $d$ -spacings matching the (200), (001), and (110) reflections of orthorhombic  $\text{V}_2\text{O}_5$ . We also observe longitudinal barcoded morphology with intermittent inorganic and organic segments (Figure 4c). As will be clarified in the next section, the organic segments are pristine bilayers of alkanethiols and the alternating dark regions (in Figure 4c) are vanadium oxide lamina.

From an aqueous HT environment, these nanorods display brownian-type bending movements of metal-oxide segments about the flexible hinges on both the nanoscale and at molecular level, as shown in Figure 5. The fabrication of nanoscale flexible hinges between vanadium oxide segments was accomplished by utilizing the layer-by-layer electrostatically self-assembly of the turbostratic thiol-intercalated  $\text{VO}_x$  nanofibers. It represents an inherent improvement to the synthetic method described by Yu *et al.*,<sup>[45]</sup> where charged nanorods are entirely encapsulated with polyelectrolytes through layer-by-layer electrostatic self-assembly.<sup>[46]</sup> Their approach entails iteratively dipping the charged nanorods in alternating baths of positive and negative polyelectrolytes to create encapsulating polymeric sheaths, beginning with a monolayer and building to a predetermined thickness with multiple layers. In this work, a new approach incorporating of the ‘sheathing’ steps is achieved during the formation of the organic-inorganic multilayered xerogel. The thiol template acts as a soft polymer sheath under nanometer thickness control facilitating flexural motion. A series of TEM images was acquired immediately after HT (Figure 5 Top), and shows the bidirectional flexing of the nanoscale hinges, which are observed to flex back and forth. The respective position of the sample cross-section with respect to the incident beam was optimized for perpendicularity by equalising the electron diffraction contribution. In this series

of images, we observe laminar bending or hinging where the vanadate lamina is observed to flex  $\pm\sim 60^\circ$ . This flexural movement is outlined schematically in Figure 4d. For nanoscale hinges, no lateral or twisting motion of the nanofibers was observed limiting the movement to the  $z$ -direction (Figure 4d) perpendicular to the  $\text{VO}_x$  lamina.

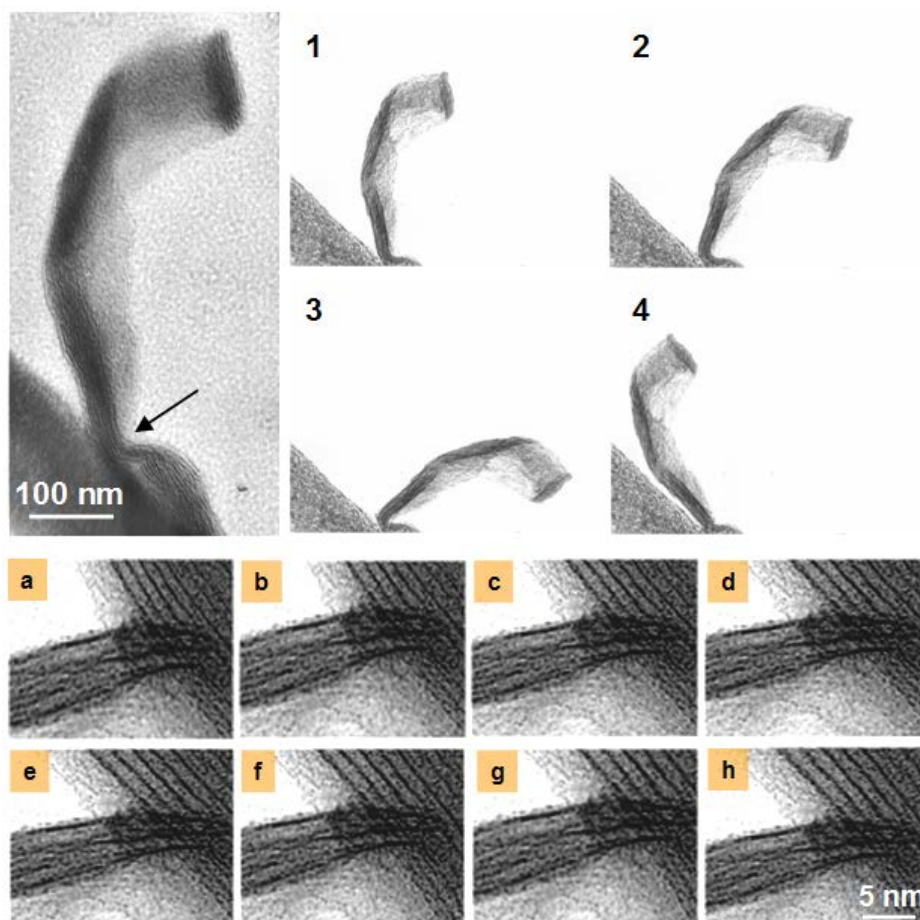


**Figure 5.** (Top): A series of TEM image snap-shots of  $\text{VO}_x\text{-(DDT)}_{0.27}$  nanofiber lamina. Lattice planes are clearly resolved through diffraction contrast. The pronounced turbostratic hinge point highlighted by an arrow was observed to undergo large-amplitude hinging as shown in images 1-4. (Bottom): A series of high resolution TEM images showing flexural hinged motion at molecular level. The images show flexing and hinging with a maximum angular divergence of  $18^\circ$ . The hinging is observed from  $65^\circ$  (a) to  $47^\circ$  (e) and back to  $63^\circ$  (h).

On the molecular level, we also observe displacement in the form of bidirectional bending of lamina only several molecular units thick (Figure 5). This series of images shows small amplitude harmonic-like flexural motion of three double bilayers of thiol-intercalated vanadium oxide. The cross-sectional TEM images again show a limited angular range of motion, to one that is perpendicular to the laminar face. A total angular displacement of  $\pm\sim 18^\circ$  is observed for the fiber segment.

The observations suggest that the relatively small-amplitude stochastic swings of the vanadium oxide segments are superimposed on a random translational brownian-like motion of the bulk nanofibers. These results suggest that the mechanical stiffness of a hinge composed of multiple

bilayers is sufficient to overcome the various forces that contribute to bending motion out of the plane of the nanofiber. A single bilayer allows the nanofiber to undergo bending vibrations about the hinge. It is quite remarkable that such a thin molecular hinge is mechanically robust enough to support such large-amplitude bending motions. Over several hours, the process was monitored and no disruption (breakage or shearing) of the hinged nanofiber was observed.

In the two examples shown, the lengths of the segments and hinges are different, thereby providing an opportunity to observe whether such alterations in the architecture of hinged nanofibers influence their movement. This seems to be the case; further work along these lines is currently in progress in order to explore the system in greater detail to further support the integration of a functional hinge into multisegmented nanofibers.

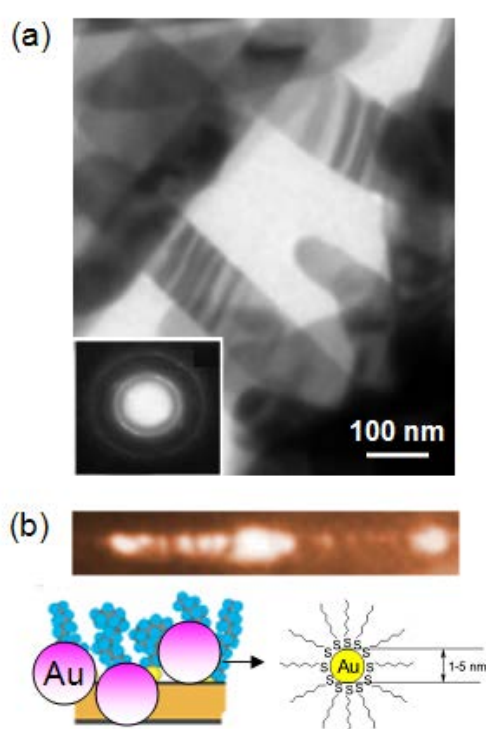


**Figure 6.** a) Bright field TEM image of  $\text{VO}_x\text{-(DDT)}_{0.27}$  nanofibers with longitudinal organic-inorganic barcoded segmentation. (Inset) SAED pattern from Au nanoparticle infiltrated nanofibers showing (111) and (220) reflections of Au. b) Higher magnification dark field TEM image acquired at the Au{111} reflection. The brilliant areas represent Au nanoparticle colloids located in the vicinity of the organic barcode segments of the nanofibers, as outlined schematically underneath.

To examine the coding capacity of the multisegmented barcoded nanofibers, Au nanoparticle colloids prepared by chemical liquid deposition, were refluxed with the nanocomposite in an ethanolic solution as described elsewhere.<sup>[12]</sup> In the bright and dark field TEM images shown in Figure 6a,b respectively, the presence of the Au nanoparticles is not clearly visible in bright field image, but by employing dark field imaging of the Au{111} reflection (Fig. 6b), brilliant points (Au nanoparticles) can be readily observed in the regions corresponding to those of lower

diffraction contrast in Fig. 6a. This observation indicates the preferential uptake of Au nanoparticles in the vicinity of the thiols, due to the affinity between the Au and the S-containing headgroups.

The system is thus amenable to guest molecule/entity uptake or docking at predetermined sites on the host lamellar nanomaterial. Obvious extensions to this would be the barcoded arrangement of luminescent dots, semiconducting nanocrystals, biological species etc., all detectable through either microscopical, chemical or non-destructive optical techniques.<sup>[47]</sup>

### 2.3. Free-Standing, Ordered Organic Nanostructures

Post-HT, we note the unique formation of organic nanofibers and nanotubes in addition to the metal-oxide nanofibers.

These structures are observed to always stem from highly barcoded organic-inorganic nanofibers such as those in Figure 7a. Bilayered dodecanethiol nanofibers are observed in the higher magnification image of Figure 7b. Organic nanostructures observed in this work have typical diameters/widths of  $\sim 25$  nm and they do not collapse under electron beam irradiation. It is of interest to note that the thiols, normally resident between the vanadate layers, delaminate (observable at several areas in Figure 7a) and become freely susceptible to bending and subsequent removal during HT in some cases.

The possibility of realizing low-dimensional organic nanostructures is a novel advance considering that, until now, only insoluble amorphous powders are actually obtained by usual electrochemical or chemical oxidation of the corresponding monomers. In cases where organic nanostructures are observed due to delamination, we observe free-standing individual organic nanofibers and nanotubes. EDX measurements (Figure 7c) of the organic nanostructure (Figure 7b) confirm the presence of thiols outside the main nanofiber structure by detection of the C content of the alkyl chains.

XPS measurements were conducted on individual organic nanostructures to confirm the presence of sulphur from the thiol head-groups and to derive semi-quantitative information on the S ordering as the outer 'skin' of the nanostructure. In the S 2p spectra (Figure 7d), a single S 2p doublet at a binding energy of  $\sim 162.0$  eV (S 2p<sub>3/2</sub>) and  $\sim 163.2$  eV (S 2p<sub>1/2</sub>) is observed relating to the bound thiolate species. The low signal-to-noise ratio of the S 2p spectra is related to the shortened acquisition time chosen to minimize any potential X-ray induced damage during the measurement. The positions and FWHM ( $\sim 1.2$  eV) of the S 2p<sub>3/2</sub> and S 2p<sub>1/2</sub> peaks are essentially equivalent to those for conventional self assembled monolayers of alkanethiols.<sup>[48]</sup> Thus, the upper surface of the thiol nanostructure (Figure 7c) is similar to a monolayer of thiols where all the S-containing head-group reside on the outside of the structure (also depicted schematically in Figure 7b). Indeed, dedicated STM measurements (Figure 7e) were acquired of the organic segment of a side-view barcoded nanofiber. The upper left of the image is the vanadium oxide and a neighbouring double bilayered arrangement of the intercalated thiols is confirmed. It is most likely that the free-standing thiol nanostructures have a similar structure, although further



work is required to determine whether the ordered organic structure is either a straight lamina bilayer or a bilayered helical architecture, both of which exhibit similar outer 'skins' of S-containing groups.

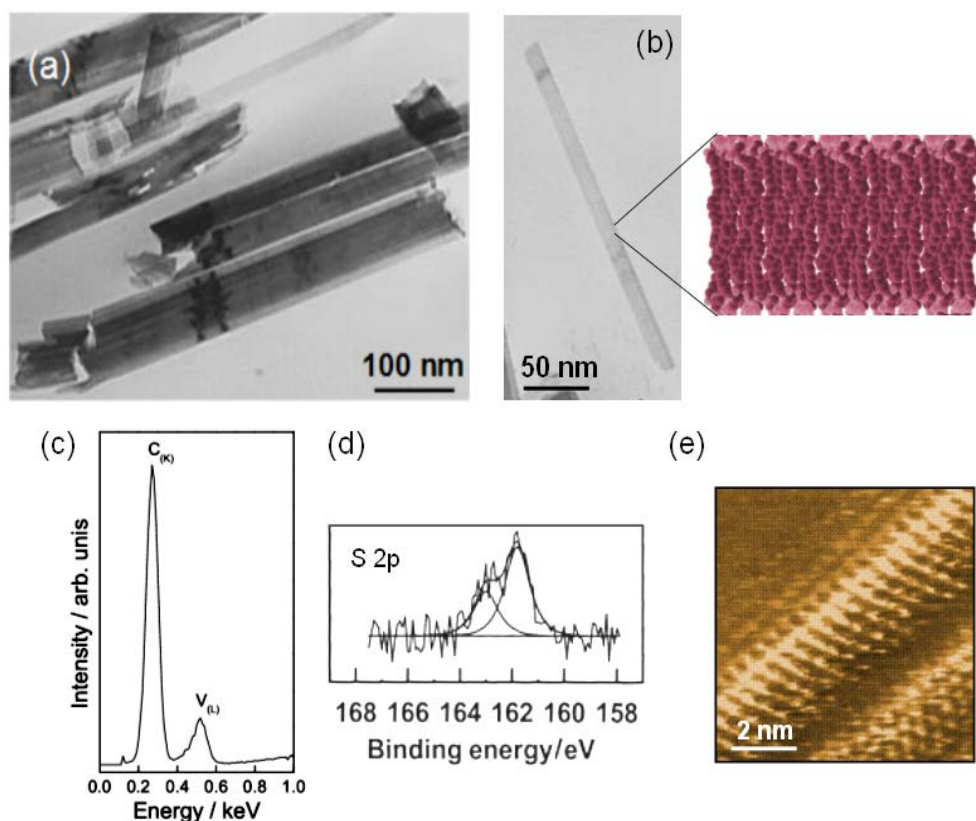


**Figure 7.** a) Bright field TEM image of  $\text{VO}_x\text{-(DDT)}_{0.27}$  nanofibers with longitudinal organic-inorganic barcoded morphology. b) Higher magnification TEM image showing a single organic nanotube. Such structures have typical diameters/widths of  $\sim 25$  nm. c) EDX spectrum of an organic nanotube showing the carbon K line and vanadium L line. d) The S 2p XPS of the organic nanotubes. The observed emission structures are fitted by a doublet Voigt function (with fixed intensity ratio of  $S\ 2p_{3/2}/S\ 2p_{1/2} = 2$  and a hyperfine splitting energy separation of 1.2 eV) related to the pristine thiolate moieties. e)  $8\ \text{nm} \times 8\ \text{nm}$  molecular resolution STM image of neighbouring inorganic-organic segments of a nanofiber cross-section in constant height mode with a sample bias of 1.5 V. Individual thiol molecules can be resolved.

#### 2.4. Defects causing Molecular Hinging, Lamina Bending and Barcoded Morphology

A series of TEM images was also acquired at specific breakage points, previously seen highlighted in Figure 4b. In addition to determining the preferential growth direction of the fibers, we also observe that the hinges stem from polymorphic deformation on the atomic scale by either cleaving of the fiber cross-sections, as seen at K (Figure 8a), or buckling of the lamina as seen at T (Figure 8b). The SAED pattern shown in Figure 8c is taken from a single nanofiber and recorded from the [100] zone axis, evidencing that the nanofibers are single crystalline with a preferential growth direction along the [010] direction, layer-by-layer in (a,c) planes. We note that on either side of breakage points, it is the vanadate layer that undergoes atomic 'ripping' although the interlaminar distance and ordering remain

intact throughout. It is these particular types of defects within the vanadate lamina that allow for the barcoded inorganic-organic periodic morphology through delamination. It is further plausible that a similar mechanism is enhanced by evaporative drying after HT; the associated shrinkage would pronounce the cleaved areas to cause delamination facilitated by breakage and/or shearing-induced mechanical strain desorption of otherwise rigidly bound thiol headgroups.

We also note that in Figure 8b, the regions highlighted by ovals are where thiols have selectively delaminated and spread to the outer edge of the nanostructure, as evidenced by the reduced diffraction contrast features. Because the amplitude and phase changes that occur when an electron is scattered elastically are characteristic of the atomic number, there will be changes in the elastic scattering directly related to the form of the projected scattering potential when there is a composition change at an interface viewed in projection by TEM, analogous to a phase grating filtering of the scattered electronic wave function.

The gaps in the atomic layers are devoid of the heavier scattering S-containing centers as well as local voids in the vanadium oxide molecular layers. Individual atomic layer bending is observed (Figure 8d) with bunched areas of locally high packing densities of S-containing head-groups at the bend points evidenced through diffraction contrast. In Figure 8d, we also observe at S a shearing of the hinge point in lamina with large curvature; to accommodate sufficient curvature to form an orthogonal bend in the overall nanofiber, shearing of the hinges occurs along the slip direction of the lamina and not out of plane angular slide motion, depicted in the schematic in Figure 8.

In this example, hinging due to buckling is further evidence of the rigidity of the thiol-templated nanofibers compared to their amine-intercalated counterparts that undergo bending and scrolling deformations during HT to form tubular nanostructures.<sup>[15]</sup> Pristine monocrystalline nanofibers are observed to grow lengthwise and the subsequent self-assembly back-to-back results in the overall fiber morphology. It is noteworthy that even considering the increased rigidity of thiol-functionalized vanadate layers as opposed to those intercalated with alkyl amines, the increase in interlaminar distance of the nanocomposite (from 2.5 to 4.9 nm as per the diffraction data) after HT, must allow for some freedom of movement of the surfactant template to allow bending and breakage, possibly due a lower degree of

alkyl chain interdigitation and interaction. In fact, the degree of bi-layered turbostratic laminarity and crystallinity of both the organic and inorganic phases is so pronounced that half-spacings (diffraction from the thiol bi-layer within the vanadium oxide bi-layer) are also observed in the SAED pattern in Figure 8c.

overall interlaminar distance and explaining the allowance for delamination. Below  $\sim 300$  K, the system is in an orientationally ordered crystalline phase. Between 300 and 370 K, it has been observed<sup>[50]</sup> that the surfactant gradually loses tilt as the temperature increases and the chains behave as hindered rotators. Above 370 K, the chains rotate more freely around their long axes and *gauche* defects form

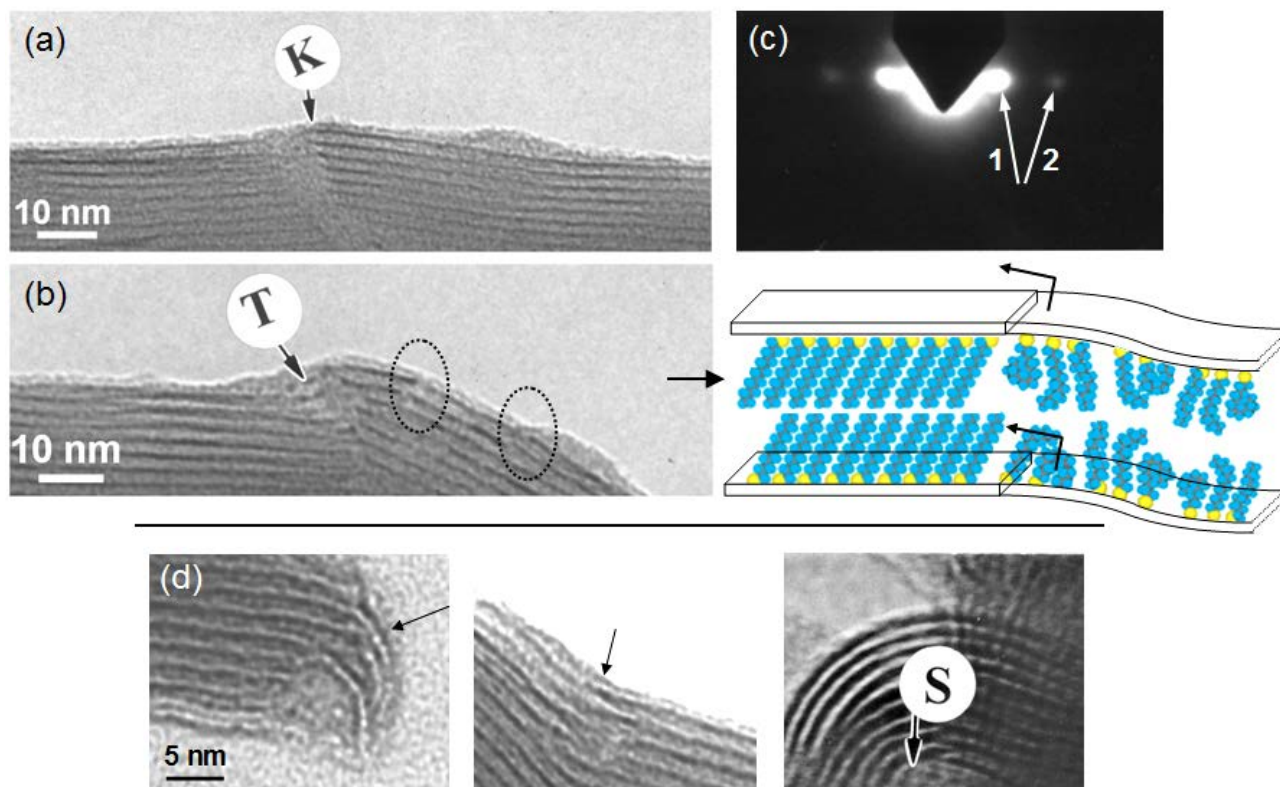


**Figure 8.** Bright field TEM images of fully developed  $\text{VO}_x\text{-(DDT)}_{0.27}$  nanofibers acquired at Scherzer (optimum) defocus near a) cleavage and b) bending deformation regions. Lattice planes are clearly resolved through diffraction contrast. c) Associated SAED pattern of the nanofibers exhibiting (1) a 4.85 nm interlaminar spacing and (2) half-spacing diffraction from the interlaminar molecular bi-layer. d) A series of TEM images of various bending and hinging of the nanofiber lamina. The higher scattering S-containing centers contribute to the darker regions (highlighted by arrows) of the interlaminar spacing by diffraction contrast. The marked oval regions indicate regions where cleavage of the lamina occurs with local removal of thiols. The schematic indicates the defective liquid-like thiol arrangement at the hinge points and the arrows indicate directions of shearing.

The rigidity is directly due to an ordered molecular template, however, the measurable amount of movement within the bi-layer itself contributes to the polymorphism and breakage observed in the nanofibers.

The  $\text{V}_2\text{O}_5 \cdot n\text{H}_2\text{O}$  xerogel is essentially a stack of ribbon-like slabs that are layers of single  $\text{V}_2\text{O}_5$  lamina consisting of edge-shared square pyramidal  $\text{VO}_5$  units, amenable to polymorphic distortion and curving. These 2D sheets are weakly bound by van der Waals forces and are readily propped open by intercalation species such as dodecanethiol in this instance. Hydrothermal treatment of the thiol-containing xerogel induces loss of bound water molecules (removal of V-OH bonds) and recrystallization of the material to orthorhombic  $\text{V}_2\text{O}_5$  during thiol bond-weakening,<sup>[49]</sup> corroborating the measured increase in

throughout the system, including kink formation and diffusion, as well as simpler motions such as *trans-gauche* isomerization. These defects allow for effective volume increases (of the defect-containing thiol molecules) and the initiation of laminar curvature, hinging and cleavage. Concurrent curvature of the metal oxide on the molecular level has shown to be theoretically possible.<sup>[51]</sup>

An increase in the interlaminar distance only occurs when tightly (chemically) bound water is removed during HT, due to the well documented condensation mechanism.<sup>[52]</sup> The cleavage of the lamina could also be attributed to the shear stress induced by the loss of coordinated water during HT recrystallization from monoclinic to the more distorted orthorhombic  $\text{V}_2\text{O}_5$ <sup>[36]</sup>, which can accommodate structural distortion and bending. The interlaminar spacing is not observed to change when only bound water that is reversibly absorbed or hydrogen-bonded is removed. The condensation forms the driving force behind the hinging observations and, during intercalation, buckling occurs preferentially (with sufficient movement allowance by the organic intercalate in this case) where the pyramidal  $\text{VO}_5$  units share only corners ( $\gamma\text{-V}_2\text{O}_5$ ). Heating, even from a 30 kV electron beam cannot be ruled out entirely, but it is unlikely since raising the temperature of an ordered alkanethiol arrangement results in a liquid-like amorphous phase without long range structural order, where in fact, the opposite is observed. We note that unlike other vanadate systems, *e.g.* amine intercalated  $\text{V}_2\text{O}_5$ ,<sup>[15,53]</sup> rolling of the laminar fibers does not occur, but rather site-specific

bending and ultimately breakage of the vanadate lamina is observed. The cleaved segments form macroscopic defects in the nanofibers leaving mainly organic molecule-containing areas segmented periodically by inorganic layers in a barcoded manner. Where crystalline cleavage does not occur, flexural motion about the hinge is caused by changes in both alkyl chain conformations and vanadate unit cell distortion from a monoclinic to orthorhombic structural phase change, resulting in bending.

### 3. Conclusions

A simple chemical route involving the hydrothermal treatment of dodecanethiol intercalated vanadium pentoxide xerogel results in the formation of monocrystalline orthorhombic  $\text{VO}_x\text{-(DDT)}_{0.27}$  nanofibers. The highly laminar xerogel readily uptakes alkanethiol molecules between vanadate atomic bi-layers. Post-HT XRD and ED studies reveal that the nanofibers are composed of stacked double bi-layers of thiol-intercalated  $\text{VO}_x$  with typical widths of 50-500 nm and lengths of typically 2-6  $\mu\text{m}$ .

An increase in the interlaminar spacing distance is observed after HT due to removal of tightly bound water molecules within the vanadate xerogel, allowing for spectroscopically detectable movement of the all-*trans* molecular bi-layer contributing to the observed bending and breakage of the vanadate atomic layers of the nanofibers.

We observe concomitant hinging of the flexible nanofiber lamina at periodic hinge points in the final product on both the nanoscale and molecular level. Barcoded nanofibers comprise alternating segments organic (thiols)-inorganic ( $\text{VO}_x$ ) material and under certain conditions free sanding bi-layered organic nanostructures are realized, improving on previously reported synthesis methods for such structures. These periodic organic-inorganic structures were shown to dock Au nanoparticles in the vicinity of the thiols. It is plausible that other guest molecules such as quantum dots or biological entities could be systematically arranged in such lamellar systems.

The layered turbostratic structure of metal-oxide nanofibers, when preserved, could provide a new organic templated-synthesis route for the fabrication of multifunctional layered nanostructures that can be functionalized for segmented nanoparticle docking sites, luminescent nanoparticle scaffolds, curved and flexible metal-oxide of organic membranes, among numerous other potential applications. With organic bilayers comprising the hinge, vanadium oxide segments can be robustly held together and undergo bending motions about the hinge. The mechanical properties of these nanostructures could see them applied in nanoscale analogues of various types of macroscale machines and devices in addition to their potential functional capability.

Although the above-described bending motion of these nanofibers is useful as a proof-of-concept idea, in addition to the structural and physical benefits of such materials, controlled bending motion of these barcoded nanofibers is needed in order to make them useful for a number of potential applications such as multifunctional transducer components and nanoscale actuators. However, modifications and extensions of the technique can be

anticipated that would enhance its capabilities, as well as potentially extending the range of applications.

### 4. Experimental Section

The vanadium pentoxide xerogel ( $\text{V}_2\text{O}_5 \cdot n\text{H}_2\text{O}$ ) was prepared from monoclinic phase  $\text{V}_2\text{O}_5$  (Aldrich). A mixture of *t*-butyl alcohol and  $\text{V}_2\text{O}_5$  was refluxed for 6 h to form the xerogel. Deionised pure water was added to the resulting dark yellow solid and the remaining *t*-butyl alcohol was removed with excess water in vacuum to yield a suspension. The material was aged at room temperature yielding a red-brown colloidal monoclinic  $\text{V}_2\text{O}_5$ . The  $\text{V}_2\text{O}_5$  and alkyl primary thiol (98%), dodecanethiol (DDT) were stirred in ethanol for 2 h in a molar ratio of 1:1, after which 20 ml of water was added and the resulting solution was agitated for 48 h at 313 K. The  $\text{VO}_x\text{-DDT}$  nanocomposite was transferred to a Teflon-lined autoclave in a sand bath and held at 313 K for several days under auto-generated pressure. Analysis of the product obtained at 313 K: Experimental (calculated for  $\text{C}_{27.6}\text{H}_{68.8}\text{S}_{2.9}\text{O}_{9.5}\text{V}_2$ : C, 44.37 (44.34); H, 9.22 (9.21); S, 12.42 (12.41).

X-ray powder diffraction characterization was performed using a SIEMENS D5000 diffractometer ( $\text{Cu K}\alpha = 0.15418 \text{ nm}$ , operation voltage 40 kV, current 30 mA). The morphological characterization was performed by field emission scanning electron microscopy (FESEM) using a JEOL JSM-6700F FESEM. Transmission electron microscopy (TEM) and selected area electron diffraction (SAED) were conducted using a Philips CM300 FEGTEM operating between 30-300 kV. Samples were mounted on holey carbon grids for structural analysis and on copper grids for EDX measurements. For snap-shot imaging of hinge movement, the accelerating voltage was reduced to 30 kV and a sample mounted directly from HT was imaged at intervals. Scanning tunnelling microscopy (STM) was conducted using a PicoSPM (Molecular Imaging, Inc.). Details on specific conditions and preparations for accurate imaging of adsorbed alkanethiolates can be found in Ref. 30. The chemical composition of the samples was determined using a SISON model EA-1108 analyzer. The Fourier transform infrared (FTIR) spectra were recorded using the KBr pellet technique with a Bio-Rad Excalibur Model FTS 3000. The XPS measurements were performed in normal emission geometry. A VG CLAM 2 spectrometer and a  $\text{Mg-K}\alpha$  X-ray source, operating at 250 W were used several centimeters from the samples. The energy scale was referenced to the Au 4f peak at 84.0 eV.<sup>[31]</sup> The spectra were normalized to the total electron yield to correct for small differences in sample positions and X-ray source intensities. The resulting spectra were fitted by using a Shirley-type background<sup>[32]</sup> and symmetric Voigt functions<sup>[33]</sup> with variable Gauss and Lorentz contributions.

### Acknowledgements

*The support of the Science Foundation Ireland (SFI) under investigator award 02/IN.1/172, the Network of Excellence PhOREMOST, the University of Chile, the Universidad Tecnológica Metropolitana, and FONDECyT Grants 1050344, 1030102, 7050081, 1050788 are gratefully acknowledged.*

- 
- [1] P. M. Ajayan, S. Iijima, *Nature* **1992**, 358, 23.
  - [2] A. M. Morales, C. M. Lieber, *Science* **1998**, 279, 208.
  - [3] Y. F. Zhang, Y. H. Tang, N. Wang, D. P. Yu, C. S. Lee, I. Bello, S. T. Lee, *Appl. Phys. Lett.* **1998**, 72, 1835.
  - [4] J. D. Holmes, K. P. Johnston, R. C. Doty, B. A. Korgel, *Science* **2000**, 287, 1471.

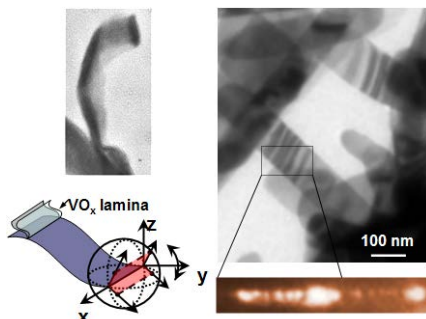
- [5] Z. W. Pan, Z. R. Dai, Z. L. Wang, *Science* **2001**, *291*, 1947.
- [6] Y. H. Gao, Y. Bando, T. Sato, *Appl. Phys. Lett.* **2001**, *79*, 4565.
- [7] Y. N. Xia, P. D. Yang, Y. G. Sun, Y. Y. Wu, B. Mayers, B. Gates, Y. D. Yin, F. Kim, H. Q. Yan, *Adv. Mater.* **2003**, *15*, 353.
- [8] P. Gomez-Romero, *Adv. Mater.* **2001**, *13*, 163.
- [9] J. F. Xu, R. Czerw, S. Webster, D. L. Carroll, J. Ballato, R. Nesper, *Appl. Phys. Lett.* **2002**, *79*, 1711.
- [10] C. Gomez-Navarro, P. J. de Pablo, J. Colchero, Y. Fan, M. Burghard, J. Gomez-Herrero, A. M. Baro, *Nanotechnology* **2003**, *14*, 134.
- [11] V. Lavayen, C. O'Dwyer, S. B. Newcomb, M. A. Santa Ana, E. Benavente, G. González, C. M. Sotomayor Torres, *phys. stat. sol. (b)* **2006**, *243*, 3285.
- [12] V. Lavayen, C. O'Dwyer, G. González, G. Cárdenas, C. M. Sotomayor Torres, *Mater. Res. Bull.* **2007**, *42*, 674.
- [13] G. T. Kim, J. Muster, V. Krstic, J. G. Park, Y. W. Park, S. Roth, M. Burghard, *Appl. Phys. Lett.* **2000**, *76*, 1875.
- [14] C. O'Dwyer, V. Lavayen, S. B. Newcomb, M. A. Santa Ana, E. Benavente, G. González, C. M. Sotomayor Torres, *J. Electrochem. Soc.* **2007**, *154*, K29.
- [15] C. O'Dwyer, D. Navas, V. Lavayen, E. Benavente, M. A. Santa Ana, G. González, S. B. Newcomb, C. M. Sotomayor Torres, *Chem. Mater.* **2006**, *18*, 3016.
- [16] C. O'Dwyer, V. Lavayen, S. B. Newcomb, M. A. Santa Ana, E. Benavente, G. González, C. M. Sotomayor Torres, *Electrochem. Solid-State Lett.* **2007**, *10*, A111.
- [17] R. Parthasarathy, J. T. Groves, *Soft Matter* **2007**, *3*, 24.
- [18] N. Kucerka, J. Pencer, J. N. Sachs, J. F. Nagle, J. Katsaras, *Langmuir* **2007**, *23*, 1292.
- [19] R. Parthasarathy, C. Yu, J. T. Groves, *Langmuir* **2006**, *22*, 5095.
- [20] A. Roux, D. Cuvelier, P. Nassoy, J. Prost, P. Bassereau, B. Goud, *EMBO J.* **2005**, *24*, 1537.
- [21] H. T. McMahon, J. L. Gallop, *Nature* **2005**, *438*, 590.
- [22] J. Zimmerberg, M. M. Kozlov, *Nat. Rev. Mol. Cell. Biol.* **2006**, *7*, 9.
- [23] A. Hultgren, M. Tanase, C. S. Chen, G. J. Meyer, D. H. Reich, *J. Appl. Phys.* **2003**, *93*, 7554.
- [24] S. R. Nicewarner-Peña, A. J. Carado, K. E. Shale, C. D. Keating, *J. Phys. Chem. B* **2003**, *107*, 7360.
- [25] M. P. Jonsson, P. Jonsson, A. B. Dahlin, F. Höök, *Nano Lett.* **2007**, *7*, 3462.
- [26] W. F. Paxton, A. Sen, T. E. Mallouk, *Chem. Eur. J.* **2005**, *11*, 6462.
- [27] G. A. Ozin, I. Manners, S. B. Fournier, A. Arsenault, *Adv. Mater.* **2005**, *17*, 3011.
- [28] S.-C. J. Huang, A. B. Artyukhin, J. A. Martinez, D. J. Sirbully, Y. Wang, J.-W. Ju, P. Stroeve, A. Noy, *Nano Lett.* **2007**, *7*, 3355.
- [29] H. Maeda, Y. Maeda, *Nano Lett.* **2007**, *7*, 3329.
- [30] C. O'Dwyer, G. Gay, B. Viaris de Lesegno, J. Weiner, *Langmuir* **2004**, *20*, 8172.
- [31] J. F. Moulder, W. E. Stickle, P. E. Sobol, K. D. Bomben, *Handbook of X-ray Photoelectron Spectroscopy* (Ed: J. Chastian) Perkin-Elmer Corporation, Eden Prairie, MN, **1992**.
- [32] D. A. Shirley, *Phys. Rev. B* **1972**, *5*, 4709.
- [33] G. K. Wertheim, M. A. Butler, K. W. West, D. N. E. Buchanan, *Rev. Sci. Instrum.* **1974**, *45*, 1369.
- [34] A. Ulman, *Chem. Rev.* **1996**, *96*, 1533.
- [35] F. Schreiber, *Prog. Surf. Sci.* **2000**, *65*, 151.
- [36] O. Durupthy, N. Steunou, T. Coradin, J. Maquet, C. Bonhomme, J. Livage, *J. Mater. Chem.* **2005**, *15*, 1090.
- [37] J. Y. Ying, A. Nakahira, D. M. Antonelli, *Inorg. Chem.* **1996**, *35*, 3126.
- [38] J. Livage, *Chem. Mater.* **1991**, *3*, 578.
- [39] V. Lavayen, M. A. Santa Ana, J. Seekamp, C. M. Sotomayor Torres, E. Benavente, G. González, *Mol. Cryst. Liq. Cryst.* **2004**, *416*, 49.
- [40] N. Pinna, M. Willinger, K. Weiss, J. Urban, R. Schögl, *Nano Lett.* **2003**, *3*, 1131.
- [41] V. Petkov, P. Y. Zavalij, S. Lutta, M. S. Whittingham, V. Paronov, S. Shastri, *Phys. Rev. B* **2004**, *69*, 085410.
- [42] M. J. Hosteller, J. J. Stokes, R. W. Murray, *Langmuir* **1996**, *12*, 3604.
- [43] W. Chen, Q. Mai, J. F. Peng, Q. Xu, Q. Y. Zhu, *J. Mater. Sci.* **2004**, *39*, 2625.
- [44] X. Chen, X. Sun, Y. Li, *Inorg. Chem.* **2002**, *41*, 4527.
- [45] J.-S. Yu, J. Y. Kim, S. Lee, J. K. N. Mbindyo, B. R. Martin, T. E. Mallouk, *Chem. Commun.* **2000**, 2445.
- [46] G. Decher, *Science* **1997**, *277*, 1232.
- [47] C. D. Keating, M. J. Natan, *Adv. Mater.* **2003**, *15*, 451; S. R. Nicewarner-Peña, G. P. Freeman, B. D. Reiss, L. He, D. J. Peña, I. D. Walton, R. Cromer, C. D. Keating, M. J. Natan, M. J. *Science* **2001**, *294*, 137.
- [48] H. A. Müller, M. Zharnikov, B. Volkel, A. Schertel, P. Harder, M. Grunze, *J. Phys. Chem. B* **1998**, *102*, 7949.
- [49] S.-M. Lee, S.-N. Cho, J. Cheon, *Adv. Mater.* **2003**, *15*, 441.
- [50] W. Mar, M. L. Klein, *Langmuir* **1994**, *10*, 188.
- [51] N. Seriani, Z. Jin, W. Pompe, L. Colombi Ciacchi, *Phys. Rev. B* **2007**, *76*, 155421.
- [52] J. Livage, M. Henry, C. Sanchez, *Prog. Solid-State Chem.* **1988**, *18*, 259.
- [53] F. Krumeich, H.-J. Muhr, M. Niederberger, F. Bieri, B. Schnyder, R. Nesper, *J. Am. Chem. Soc.* **1999**, *121*, 8324.

Received: ((will be filled in by the editorial staff))  
Published online on ((will be filled in by the editorial staff))

## Entry for the Table of Contents (Please choose one layout)

Layout 1:

Both low-dimensional barcoded metal-oxide layers that exhibit molecular hinging and free-standing ordered organic nanostructures can be obtained from unique nanofibers of vanadium oxide. Barcoded nanofibers comprise alternating segments of organic(thiols)-inorganic( $\text{VO}_x$ ) material and are amenable to selective nanoparticle uptake.



full

### Flexible Nanostructures

C. O'Dwyer, V. Lavayen,  
D. Fuenzalida, H. Lozano, M. A.  
Santa Ana, E. Benavente, G.  
González, C. M. Sotomayor  
Torres \_\_\_ Page No. – Page No.

**Low Dimensional Hinged Barcode  
Metal Oxide and Free-Standing  
Ordered Organic Nanostructures  
from Turbostratic Vanadium Oxide**